2024 IEEE/RSJ International Conference on Intelligent Robots and Systems (IROS)
October 14-18, 2024. Abu Dhabi, UAE

Shadow Maintenance for Automatic Light-Probe Control in Ophthalmic Surgeries Using Only 2D information

Junjie Yang[1], Satoshi Inagaki[2], Zhihao Zhao[1], Daniel Zapp[3], Mathias Maier[3], Kai Huang[5],
Nassir Navab[1], *Fellow, IEEE*, and M. Ali Nasseri[3,4]

***Abstract*— In ophthalmic surgeries, the light probe is responsible for providing safe intraocular illumination and ensuring the visibility of the instrument and its shadow as the only available reference for qualitative depth estimation and landing point prediction in fundus microscopic images. To achieve sustainable shadow-based estimation during surgeries, we propose controlling the light probe automatically to limit the shadow position around the instrument tip using only 2D information from the microscope. We also integrate an intensity balancing sub-module to guarantee the normal intensity distribution and the safe depth of light-tip placement. Without motor-based pose coordination between the light probe and the instrument, experiments analyze the performance of our image-based shadow maintenance with only image information under the constraints of RCM and discuss the working volume and segmentation limitations during simulation and real-robot tests.**

I. INTRODUCTION

In ophthalmic surgeries, surgeons coordinate a light probe and a surgical instrument (i.e., a needle) under a microscope for intraocular manipulations, as depicted in Fig. 1. During the surgical procedure, surgeons pivot the light probe to provide sufficient intraocular illumination and activate essential visual effects, such as the instrument shadow around the needle tip, to help estimate the needle-tip depth, predict the landing point, and adjust the relative position between the needle and intraocular targets [1]–[6]. Meanwhile, surgeons prevent the light probe from collisions with the retina and light toxicity. Therefore, due to its crucial role in providing intraocular illumination and aiding in needle positioning, the light probe's control remains formidable, mainly when relying solely on 2D information from the microscope.

Recently, novel imaging modalities, such as intraoperative Optical Coherence Tomography (iOCT), have been introduced for surgeons' intraocular 3D perception during eye surgeries [7]–[13]. However, their deployment is limited to specific interventions such as subretinal injection, where its 3D perception supplants the light probe within the surgical region of interest (ROI). Other research proposes using laser- and structured light-based probes to cast visual target indicators on the retina for needle navigation [14]–[17], which sacrifices the light probe's illumination and shadow-casting functions and requires additional safety-concerned modalities like force sensors. Thus, despite the emergence of alternative probes, the traditional light probe retains its indispensability, and its automated control methods bridge the gap between manual and fully automated ophthalmic surgical procedures.

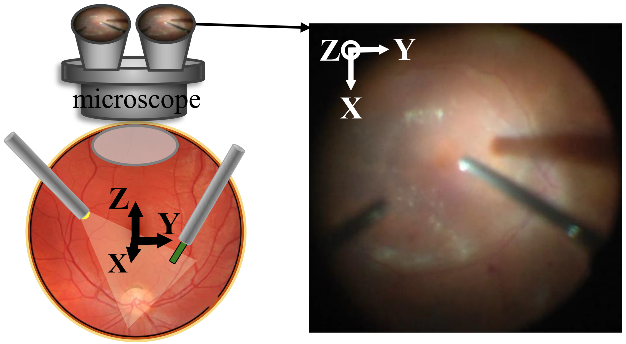

Fig. 1: A typical setup of ophthalmic surgeries.

As for automatic light-probe control, most existing methods establish a universal robotic framework to achieve the light probe and the needle's cooperation within the same coordinate system [18]–[20]. Consequently, they obtain the pose transformation matrix using real-time kinematic data from motor encoders in a universal coordinate. However, such fully-automated robot-assisted surgeries require much priors, such as two-robot calibration and coordination, which is not suitable for the current manual manipulations that rarely provide simultaneous instrument poses. Therefore, solutions are needed to compensate for the compatibility of automatic light-probe control with manually controlled instruments in the current surgical context.

Addressing the concerns above, we propose using the shadow position to drive the light probe's automatic shadow maintenance in a 12mm-radius eyeball model. This paper analyzes the relative light-needle position to define the light probe's limited position range for shadow maintenance. This method also balances the light intensity of ROI areas to avoid light toxicity and tissue damage. Experiment results show the procedure of adjusting shadow and distributing light intensities. The contributions of this paper are listed: 1) an image-only shadow-maintenance method; 2) integration of intensity balance to avoid retina damage; 3) safety and working-volume analysis.

[1] School of Computation, Information and Technology, Technical University of Munich, 80333 Munich, Germany {junjie.yang,zhihao.zhao,nassir.navab}@tum.de

[2] NSK Ltd., 141-0032 Tokyo, Japan inagaki-s@nsk.com

[3] Klinik und Poliklinik für Augenheilkunde, Klinikum rechts der Isar, 81675 Munich, Germany {daniel.zapp,mathias.maier}@mri.tum.de, ali.nasseri@tum.de

[4] Department of Biomedical Engineering, University of Alberta, T6G 2R3 Edmonton, Canada.

[5] School of Computer Science and Engineering, Sun Yat-Sen University, 510006 Guangzhou, China huangk36@mail.sysu.edu.cn

979-8-3503-7769-9/24/$31.00 ©2024 IEEE

II. METHOD

A. *Basics*

Assume that all surgical components, including light-probe tip p_{ltip}, needle tipp_{ntip}, and shadow tip p_{stip}, are visible within the retina area. The microscope-eyeball alignment also holds during the surgery. In this paper, the default control parameters for 512x512 microscope frames can be scaled and fine-tuned for other image sizes.

In ophthalmic surgery, as insertion tunnels for instruments, trocars become the center of all instrument movements, forming the remote center of motion (RCM) principle within a spherical coordinate system. This principle allows for three fundamental instrument motion candidates: vertical rotation (polar, VRCM), horizontal rotation (azimuthal, HRCM), and axial insertion (radius, ZOOM), as presented in Fig. 2(a)-(c).

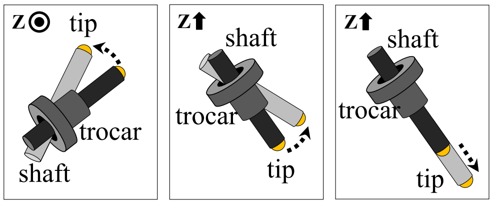

(a) HRCM. (b) VRCM. (c) ZOOM.

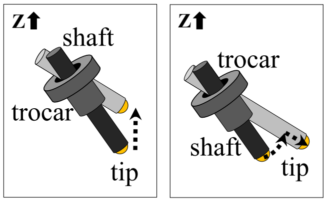

(d) UPDW. (e) FOWD.

Fig. 2: The light probe's RCM motion candidates.

Furthermore, the combination of fundamental motions can generate other particular instrument-tip trajectories. Assume that the VRCM is aligned inside the vertical plane without horizontal deviation. Since VRCM motion causes visual changes in axial length, ZOOM is needed to compensate for the insertion length to fix the needle tip around the target planar point (i.e., UPDW-up from VRCM-up plus ZOOM-out as depicted in Fig. 2(d)). Forward exploration movement (FOWD), as in Fig. 2(e), is also a combination of VRCM and ZOOM. Meanwhile, FOWD enlarges the axial change caused by VRCM by ZOOM in the same direction of deviation (i.e., FOWD-up from VRCM-up plus ZOOM-in). Then, we use the five motion candidates in Fig. 2 to actuate the light probe.

B. *Depth for Shadowing*

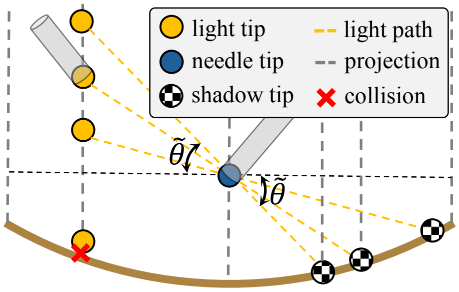

Fig. 3: In the shadowing plane that is perpendicular to the imaging plane, the light probe tip's horizontal level determines the projected shadow-tip position on the retina in the imaging plane (x-y plane).

According to the principle of shadowing, the light-probe tip p_{ltip}, the needle tip p_{ntip}, and its shadow tip p_{stip} are on the same line in the 3D space, which determines a plane that encompasses this line and is perpendicular to the imaging plane, as shown in Fig. 3. Considering an undistorted intraocular image with ideal liquid density distribution, this light-instrument-shadow line holds in the image, which is an assumption of this paper.

The light path from the light-probe tip to the shadow tip intersects the needle tip's horizontal level, making the angle $\tilde{\theta}$ as Equation (1). p^{xy} is the projection of p in the x-y plane.

$$\begin{aligned} \Delta_{xy} &= \sqrt{(p_{ltip}.x - p_{ntip}.x)^2 + (p_{ltip}.y - p_{ntip}.y)^2} \\ \Delta_z &= p_{ltip}.z - p_{ntip}.z \\ \tilde{\theta} &= \text{atan}(\frac{\Delta_z}{\Delta_{xy}}) \end{aligned} \tag{1}$$

Then, the light-probe tip's movement and the corresponding shadow-tip variation on the retina can be described by $\tilde{\theta}$ in the image and the 3D space.

- $\tilde{\theta}\uparrow$: $p_{ltip}.z \uparrow$ and $\lim \|p^{xy}_{ntip} - p^{xy}_{stip}\| \rightarrow 0$
- $\tilde{\theta}\downarrow$: $p_{ltip}.z \downarrow$ and $\lim \|p^{xy}_{ntip} - p^{xy}_{stip}\| \leqslant 2 * r_{eye}$.

Meanwhile, the eyeball shape (radius r_{eye}) and the shadow tip's visible range (radius r_{vis}) bounds the light probe's vertical position. As for the light-eyeball collision, the light-probe tip should obey Equation (2).

$$p_{ltip}.z^{le/he} = \pm\sqrt{r_{eye}^2 - p_{ltip}.x^2 - p_{ltip}.y^2} \tag{2}$$

As for shadow visibility, the light-probe tip's lowest position follows Equation (3) where p_{stip} is at the visible edge.

$$\begin{aligned} r_{vis} &= \sqrt{p_{stip}.x^2 + p_{stip}.y^2} \\ \tilde{\theta} &= \text{atan}(\frac{p_{ntip}.z - p_{stip}.z}{\|p^{xy}_{ntip} - p^{xy}_{stip}\|}) \\ p_{ltip}.z^{ls} &= p_{ntip}.z + \tan(\tilde{\theta}) \cdot \|p^{xy}_{ltip} - p^{xy}_{ntip}\| \end{aligned} \tag{3}$$

Furthermore, the light-probe tip should also obey Equation (4) to avoid needle-shadow visual overlapping.

$$\begin{aligned} \sigma^{min}_{stip2ntip} &= \|p^{xy}_{stip} - p^{xy}_{ntip}\| \\ \tilde{\theta} &= \text{atan}(\frac{p_{ntip}.z - p_{stip}.z}{\|p^{xy}_{ntip} - p^{xy}_{stip}\|}) \\ p_{ltip}.z^{hs} &= p_{ntip}.z + \tan(\tilde{\theta}) \cdot \|p^{xy}_{ltip} - p^{xy}_{ntip}\| \end{aligned} \tag{4}$$

Overall, the position boundary of the light-probe tip should obey Equation (5). However, the eye-based bounds

$p_{ltip}.z^{le/he}$ have the highest priority during surgeries to avoid tissue damage.

$$\begin{aligned} p_{ltip}.z^{high} &= \min(p_{ltip}.z^{hs}, p_{ltip}.z^{he}) \\ p_{ltip}.z^{low} &= \max(p_{ltip}.z^{ls}, p_{ltip}.z^{le}) \end{aligned} \tag{5}$$

Considering the light probe's cone-shaped light range, the shadow should form an apparent contrast against the lighted retina for visual recognition and segmentation. The local tissue deformation around the trocar also limits the light-probe rotation. Although these considerations need future thorough discussion, we only update (5) to position the light probe in this paper for shadow placement.

C. Shadow Placement

This paper achieves the light probe's control task by limiting the visible shadow tip p_{stip} within the desired shadow area around the visible needle tip p_{ntip}, as shown in Fig. 4 with the used parameters listed in Table I.

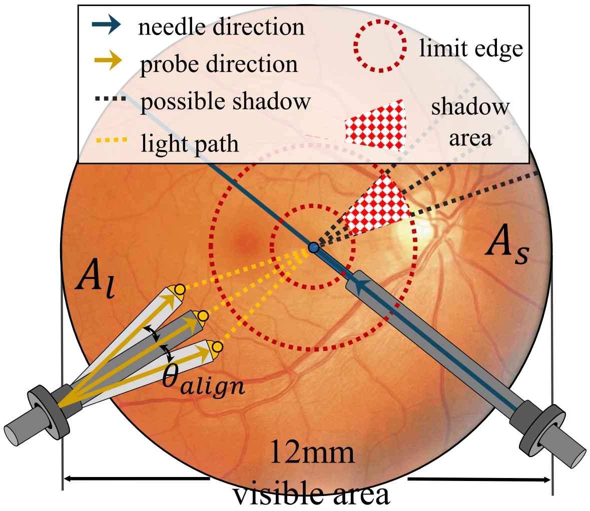

Fig. 4: The area division during the proposed shadow placement (radius r_{vis} = 6 mm).

This shadow placement contains two steps: **horizontal alignment** and **vertical maintenance**. The **horizontal alignment** is to horizontally rotate the light probe to make its projected orientation toward the needle tip within the angle threshold θ_{align}. The shadow position is acceptable sporadically, even if the light-probe orientation (direction of casting light) is not towards the needle. However, the potential improper distribution of light on the retina makes the shadow area too dark to extract the tip. Therefore, **horizontal alignment** allows a coarse-grained value tuning of θ_{align}.

The next step **vertical maintenance** is to position the shadow tip within the desired shadow area around the needle tip. By replacing r_{vis} in (3) with a maximal threshold $\sigma^{max}_{stip2ntip}$, an outer limit edge, as marked in Fig. 4, is defined to ensure that the shadow tip is around the needle tip for estimating the needle tip's landing point on the retina. Accordingly, the shadow-based lower bound $p_{ltip}.z^{ls}$ in Equation (5) is also updated. Meanwhile, overlapping the needle tip p_{ntip} and its shadow tip p_{stip} may cause a visual needle-shadow intersection before the needle tip touches the retina. Therefore, the threshold $\sigma^{min}_{stip2ntip}$ defines the inner limit edge in Fig. 4 to keep p_{stip} slightly deviated from p_{ntip}, allowing additional space to check the needle-retina distance manually, as described by (4).

TABLE I: Planar Parameters for Shadow Placement

variable	function	value
θ_{align}	horizontal alignment	10.0°
$\sigma^{min}_{ltip2ntip}$	minimal $d_{ltip2ntip}$	20 pixels
$\sigma^{max}_{ltip2ntip}$	maximal $d_{ltip2ntip}$	300 pixels
$\sigma^{min}_{stip2ntip}$	minimal $d_{stip2ntip}$	10 pixels
$\sigma^{max}_{stip2ntip}$	maximal $d_{stip2ntip}$	100 pixels

As depicted in Fig. 4, the needle's center line l_{ntip} divides the visible retina area into two parts: A_l as the range of p_{ltip} and A_s as the range of p_{stip}. $p_{ltip} \in A_l$ maintains its distance from p_{ntip} as $d_{ltip2ntip} \in [\sigma^{min}_{ltip2ntip}, \sigma^{max}_{ltip2ntip}]$ after the horizontal alignment, which guarantees no light-needle collision during the shadow placement procedure.

The overall shadow placement is presented in **Algorithm 1**. $\vec{v}_{ltip}$ is the light-probe orientation vector, and $\vec{v}_{ltip2tip}$ is the direction vector from the light-probe tip toward the needle tip. Δ^{dir}_{motion} is the step angle/length of a motion along the given direction. This control procedure should be paused with manual intervention when the light-probe tip disappears in the visible range. Function IntensityBalance() is described in the next section.

Algorithm 1 Shadow Placement

```
$\theta$ = intersec($\vec{v}_{ltip}$, $\vec{v}_{ltip2ntip}$)
if $\|\theta\| > \theta_{align}$ then HRCM($\theta$, $\Delta_{HRCM}$)
else
    $d_{ltip2ntip}$ = dis($p_{ltip}$, $p_{ntip}$)
    if $d_{ltip2ntip} < \sigma^{min}_{ltip2ntip}$ then FOWD($\Delta^{down}_{FOWD}$)
    elif $d_{ltip2ntip} > \sigma^{max}_{ltip2ntip}$ then FOWD($\Delta^{up}_{FOWD}$)
    else
        if $p_{stip}$ not visible then UPDW($\Delta^{up}_{UPDW}$)
        else
            $d_{stip2ntip}$ = dis($p_{stip}$, $p_{ntip}$)
            if $d_{stip2ntip} > \sigma^{max}_{stip2ntip}$ then UPDW($\Delta^{up}_{UPDW}$)
            elif $d_{stip2ntip} < \sigma^{min}_{stip2ntip}$ then UPDW($\Delta^{down}_{UPDW}$)
            else IntensityBalance()
```

D. Balance of Intensity

With an acceptable shadow position, the light-probe tip risks damaging the retina by light toxicity [21] and potential collision. In this case, the light probe shapes a small retinal area with over-strong light intensity around the light-probe tip while making the rest area too dark. Therefore, it is necessary to keep the distance between the light probe and the retina within a reasonable range [22]. Therefore, a intensity balance algorithm is adopted, as shown in Fig. 5.

Considering the lighting path $l_{ltip2stip}$ from p_{ltip} to p_{stip}, we define the area around a tip along $l_{ltip2ntip}$ with radius σ_{ROI} as the ROI of measuring and balancing light intensities.

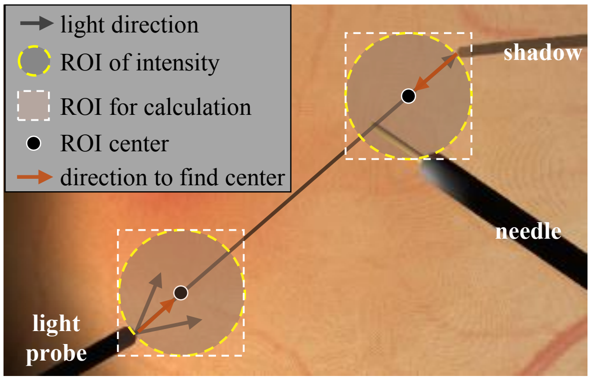

Fig. 5: The ROI areas for intensity calculation and balancing.

TABLE II: Parameters for Intensity Balance

variable	function	value
σ_{ROI}	radius of ROI for intensity	30 pixels
σ_{ltip}^{max}	maximal intensity I_{ltip}	170
σ_{gap}	maximal intensity gap between ROIs	20

Ideally, we calculate the average light intensity of the ROI area after RGB-grayscale conversion using parameters in Table II. We replace the circle ROI with its circumscribed square to simplify coding. After obtaining the light-probe tip's ROI intensity I_{ltip} and the shadow tip's ROI intensity I_{stip}, intensity balancing, as presented in **Algorithm 2**, runs to ensure:

- $I_{ltip} <= \sigma_{ltip}^{max}$ to avoid collision and toxicity.
- $abs(I_{ltip} - I_{stip}) <= \sigma_{gap}$ to generate clearer shadows.

Algorithm 2 Intensity Balance

```
$p_{center}^{ltip} = p_{ltip} + \sigma_{ROI} * \vec{v}_{ltip2stip}$
$p_{center}^{stip} = p_{stip} - \sigma_{ROI} * \vec{v}_{ltip2stip}$
$I_{ltip}$ = GetAverage($p_{center}^{ltip}$, $\sigma_{ROI}$)
$I_{stip}$ = GetAverage($p_{center}^{stip}$, $\sigma_{ROI}$)
if $I_{ltip} > \sigma_{ltip}^{max}$ then UPDW($\Delta_{UPDW}^{up}$)
else
    if $\|I_{ltip} - I_{stip}\| > \sigma_{gap}$
        if $I_{ltip} < I_{stip}$ then VRCM($\Delta_{VRCM}^{down}$)
        else VRCM($\Delta_{VRCM}^{up}$)
    else WaitForNextFrame()
```

Function GetAverage() obtains the average grayscale intensity of the ROI area defined by p_{center} and σ_{ROI}. The VRCM rotation is adopted to optimize the intensity distribution along the light-shadow segment.

III. SIMULATION AND ANALYSIS

A. Simulation Test

1) Setup: We use a private Unity-based simulator, as shown in Fig. 6, to generate microscope frames (512x512 pixels at 50 fps) and corresponding ground-truth position data (p_{ltip}, p_{ntip}, p_{stip} and light orientation $\vec{v}_{ltip}$). The step angle rotation and the step translational movement are 0.5° and ∼0.067 mm, respectively. The needle's trocar is at $[4.5, 8.0, 8.0]$ while the light probe's trocar is installed at 4 positions: $[8.0, -4.5, 8.0]$, $[4.68, -7.90, 8.0]$, $[0.10, -9.18, 8.0]$, $[-4.5, -8.0, 8.0]$. By connecting the trocar with the planar eye center, two lines of two trocars to the center form a list of angles $[90.0, 120.0, 150.0, 180.0]$ (degrees). These angles help analyze which trocar installation position should be selected to ensure successful shadow maintenance within a specific retina area.

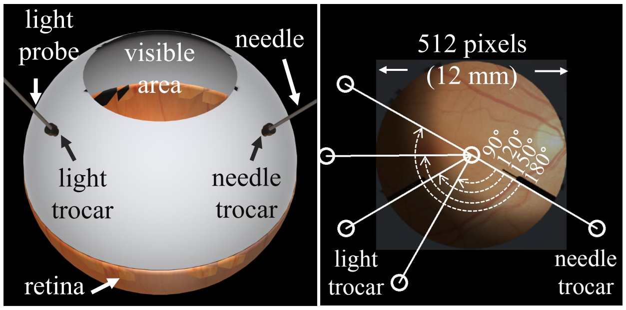

Fig. 6: The simulator for performance assessment.

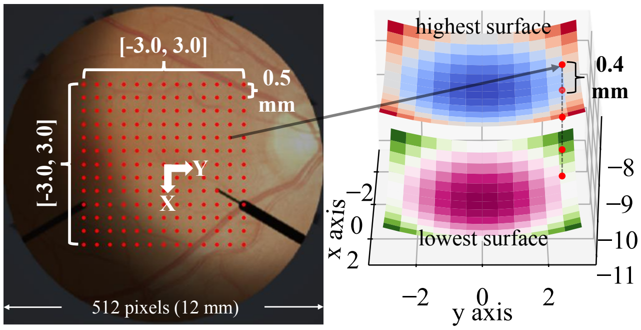

Fig. 7: The design of processing rasterized needle tips.

We mainly test the 6x6 mm^2 square center area as the common area of targets in eye surgery. In the planar xy plane, we rasterize the above-retina area ($[-3.0, 3.0]$ along x-/y-axis) into 13x13 points with granularity $\Delta_{x/y} = 0.5$ mm, as shown in Fig. 7. As for the z-axis, we generate 5 above-retina points with granularity $\Delta_z = 0.4$ mm and distance $[0.4, 0.8, ..., 2.0]$. Then, the above-retina space is rasterized into 845 points to place the needle tip. This paper only considers the shadow-based tool-retina distance maintenance, and hence, analyzes a 2.0-mm distance from the retina. Once the needle tip goes higher than 2.0 mm from the retina, it is regarded as a safe procedure of instrument navigation without concerns of safe distance maintenance. During simulation, the following cases are considered failures: 1) no success feedback from the controller after 5-second running; 2) distance $d_{ltip2retina} \leqslant 2.0$ mm; 3) distance $d_{ltip2ntip} \leqslant 2.0$ mm.

Using the above-mentioned setup, we manually put the needle tip at each rasterized point, and automatically control the light probe using the proposed algorithms in a RCM-compatible environment.

2) Results: The successful ratio distributions in all height levels with different trocar angles are presented in Fig. 8. During simulation, the failures in each above-retina height are symmetrically distributed along the diagonal due to the symmetric spherical surface of the retina.

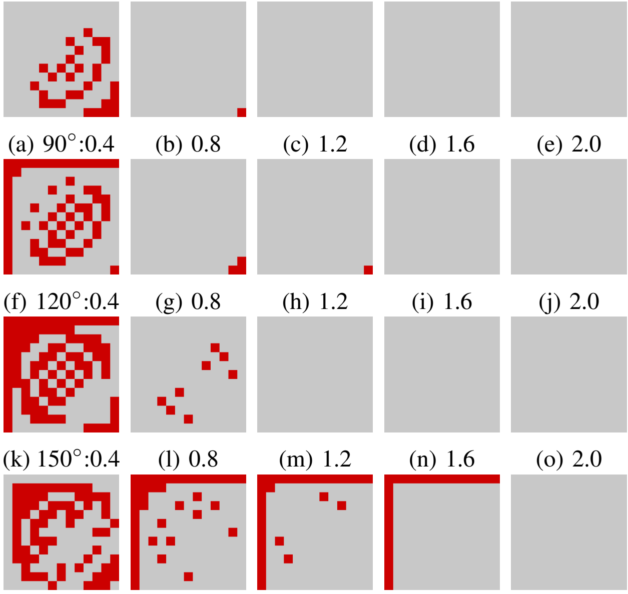
(a) 90°:0.4 (b) 0.8 (c) 1.2 (d) 1.6 (e) 2.0

(f) 120°:0.4 (g) 0.8 (h) 1.2 (i) 1.6 (j) 2.0

(k) 150°:0.4 (l) 0.8 (m) 1.2 (n) 1.6 (o) 2.0

(p) 180°:0.4 (q) 0.8 (r) 1.2 (s) 1.6 (t) 2.0

Fig. 8: The result of needle-tip points in all above-retina heights of different trocar placement angles (red is failure).

For a given trocar installation angle, the success ratio increases when the needle tip gets further from the retinal surface. According to Equation (5), when the light-probe tip moves a unit distance, the shadow tip's planar deviation is smaller when the needle tip is closer to the retina. When the needle tip is closer to the retina in the range $[0.4, 2.0]$, it requires more vertical distances for the light probe to separate the projected shadow tip from its needle tip. This required z-axis movement makes the light probe approach to the retina too fast, which may cause light-retina collision risk and light toxicity.

For a given above-retina height, the success ratio decreases as the trocar intersection angle increases from 90° to 180.0°. When two instruments make an orthogonal orientation intersection, the shadow is cast along the light path as the fastest planar direction for needle-shadow separation. By contrast, when two trocars form almost 180°, it is easy for the instruments to share the same center line, casting the shadow beneath the needle shaft. This visual needle-shadow overlapping requires the light probe's horizontal alignment instead of vertical movements to finish the visual separation, as discussed in [18]. However, the horizontal alignment moves the light-probe orientation away from the needle tip, leading to weaker intensity distribution along the light-needle path $l_{ltip2ntip}$ and hence the difficulty of shadow recognition.

Combining the analysis above, we find that 90° surpasses other trocar angles to obtain a higher success ratio and a larger vertical range of shadow maintenance using the current hyper-parameters. This trocar angle can be further analyzed by adopting smaller angle granularities. We also observed the conflict between shadow maintenance and intensity balance during the execution, which caused a timeout (10 seconds for each target) and, consequently, failure. For example, the competition between FOWD-down (for reducing light-needle distance) and VRCM-down (for balancing intensity) keeps the light probe's tip swinging at the border distance $\sigma^{max}_{ltip2ntip}$. Such types of failures should be resolved by assigning reasonable execution priorities to the shadow maintenance and intensity balance and dynamically tuning the distance thresholds in the future.

We also collect the distances among the light-probe tip, the needle tip, and the retina surface, as presented in Fig. 9, to illustrate the safety of automatic shadow maintenance. As for the light-needle distances in Fig. 9(a)-(d), the main distribution is located around 10 mm, which is safe for light-needle coordination. The distances in successful cases are $\geqslant$ 6 mm, while there are still failure cases to have risky distances within $[0.0, 1.0]$ mm. These improper distances are monitored by the robot and the surgeon for necessary interruption of automatic control during the surgery. As for the light-retina distances in Fig. 9(e)-(h), the main distribution is also located around 10 mm, which avoids collision and tissue damage. However, in the case of 180° trocar intersection angle, there are a noticeable amount of failures, as shown in Fig. 9(h), with the risk of dangerous light-retina distance (within $[0.0, 2.0]$ mm) or unexpected collisions, making 180° not recommended to be the trocar installation angle within the context of current parameters.

TABLE III: Vertical Working Volume (Polar Angle)

Trocar Angle	**Min**	**Max**	**Range**
90°	149.35	165.35	16.00
120°	150.36	165.86	15.50
150°	151.38	162.88	11.50
180°	145.85	165.85	20.00

The corresponding working volume represented by the light probe's polar angle in the vertical plane is listed in Table III for all target needle-tip points. The current hyper-parameters generate a range of $[10.0^\circ, 20.0^\circ]$ varying along with the trocar intersection angle. The required vertical working volume provides a reference for the robot design in the vertical RCM plane. It also helps determine the initial pose of the light probe to cover both upward and downward VRCM rotations, which is meaningful for future research on deploying the robot controller in the surgical room.

B. Robot Test

Using a 3-DoF robot to control the light probe, as presented in Fig. 10, a simple qualitative test on an open-sky eye phantom illustrates the procedure of shadow maintenance

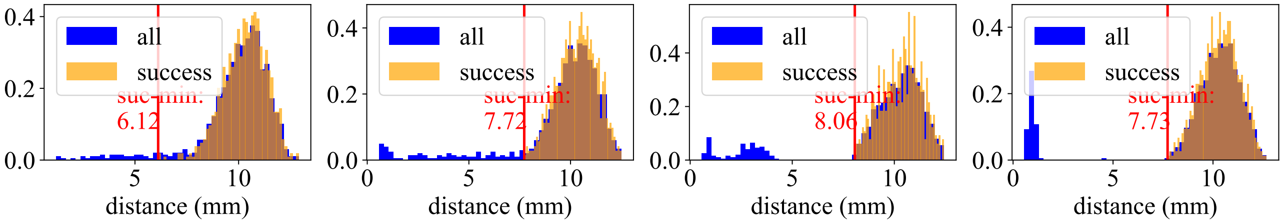

(a) 90° (light-needle). (b) 120° (light-needle). (c) 150° (light-needle). (d) 180° (light-needle).

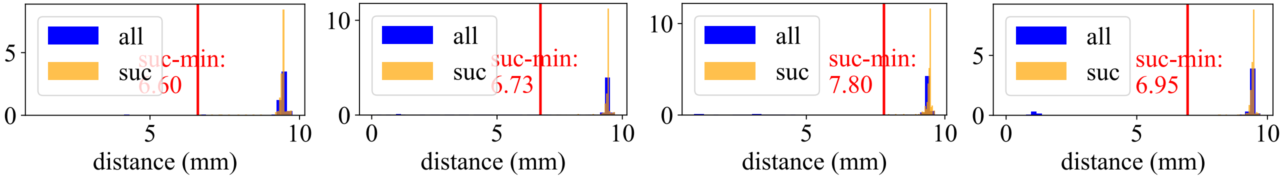

(e) 90° (light-retina). (f) 120° (light-retina). (g) 150° (light-retina). (h) 180° (light-retina).

Fig. 9: The distances between objects with different trocar placement angles.

without precise trocar fixation on the phantom. Despite external light factors, the light probe's solid illumination is still the dominant source to shape instrument shadows. We directly consider the last three joints (d_3, t_4, and d_5) to verify the method only in the vertical plane, which is compatible with the motion features of shadow maintenance and intensity balance. The theoretical range of RCM rotation in the vertical plane is around $[-9.0°, 9.0°]$ to cover 18°.

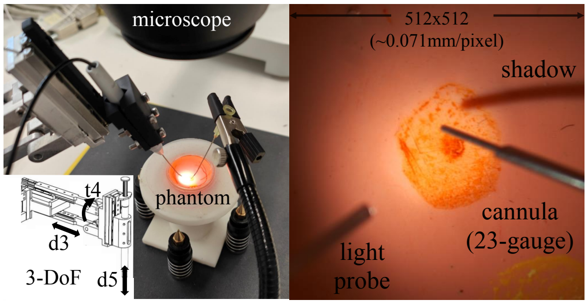

Fig. 10: The hardware setup for qualitative test.

TABLE IV: Segmentation Metrics

Model	**Num (Train)**	**Num (Valid)**	**Batch**
Yolov8l-seg	149	37	16
Epoch	**Precision**	**mAP50**	**mAP50-95**
291	0.9858	0.9829	0.6429

We simply test the shadow-maintenance concept with the procedure depicted in Fig. 11 using YOLOv8 [23] as the segmentation tool. The training information is listed in Table IV, which demonstrates a prior segmentation precision before subsequent tool orientation and tip extraction in this experiment. In practical surgery scenarios, a higher segmentation precision is a necessity for the deployment of such image-guided control algorithms. Due to the limitation of the actuator, we manually ensure the horizontal alignment. Considering the instability of segmentation, we enlarge the threshold $\theta_{align} = 10.0$ to keep the horizontal orientation.

As shown from Fig. 11(a)-(e), by conducting the UPDW-up motion on the light probe (yellow), the shadow tip (red) gradually moves closer to the needle tip (green) based on the prior orientation alignment. Simultaneously, the decrease of strong light intensity around the light-probe tip (red circle area) can be clearly recognized, generating a more uniform light distribution between the light-probe tip and the shadow tip. However, the segmentation error in Fig. 11(f) leads to an emergency pause of the light probe control to avoid tissue damage, which emphasizes the necessity of enhancing segmentation for more accurate and precise segmentation results and subsequent image-based control methods.

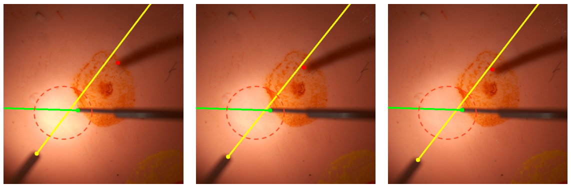

(a) UPDW-1. (b) UPDW-2. (c) UPDW-3.

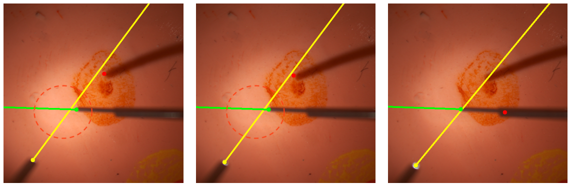

(d) UPDW-4. (e) UPDW-5. (f) Error.

Fig. 11: The runtime procedure of shadow-maintenance by UPDW motion using a 3DoF robot.

IV. DISCUSSION AND CONCLUSION

This paper aims to maintain the visibility of essential visual components in the microscope for a safe tool-retina interaction and tests this concept using simulation and open-sky eyes. Instead of requiring function execution throughout the surgery, this paper provides an area of placing the shadow and still allows for manipulation tasks by temporarily holding the light static according to surgeons' simultaneous schedule, which prevents interfering human decisioning. Meanwhile, this method is still challenged by three major problems: 1) real-surgery image processing, 2) module scheduling priorities, and 3) control frequency bounding.

In actual vitreoretinal surgeries, image segmentation should be accurate and precise for object extraction and subsequent tool navigation, which is still a challenging task and requires human supervision and intervention. Also, the rotated eyeball posture will influence the illumination and the extraction of geometrical information, leading to a limited retinal ROI in this paper. Next, improper module priority also creates deadlocks of controlling logic, which causes the light probe's oscillation and generates unstable shadow tips on the retina to interfere with surgeons' decisions with a static needle tip. Furthermore, we only test the performance of shadow maintenance for static needle-tip points with 20-50 Hz frame processing (including image segmentation on an RTX A5000 card). It is critical to bound the control frequency of the light probe to ensure that the shadow-maintenance result can be generated and kept in time when the needle tip moves continuously inside the eye. Last, the performance of shadow maintenance is heavily bonded with the trocar position and target retina areas, which requires more detailed analysis in real eyes.

In conclusion, automatic light-probe control is promising but challenging for enhancing surgical automation, especially with the expensive cost of introducing additional robot arms. With the motivation of less prior acquisition (i.e., real-time instrument pose) during surgeries, we will continue improving image-based shadow maintenance and light-instrument coordination in more realistic environments.

ACKNOWLEDGEMENT

The authors thank SynthesEyes for its assistance during simulations and robotic experiments.

REFERENCES

[1] E. Sugisaka, K. Shinoda, S. Ishida, Y. Imamura, Y. Ozawa, T. Nakajima, H. Shinoda, K. Suzuki, N. Kawaguchi, and M. Inoue, "Visual sensations during vitrectomy," *Ophthalmology*, vol. 113, no. 10, pp. 1886.e1–1886.e3, Oct. 2006. [Online]. Available: http://dx.doi.org/10.1016/j.ophtha.2006.02.013

[2] R. S. Ajlan, A. A. Desai, and M. A. Mainster, "Endoscopic vitreoretinal surgery: principles, applications and new directions," *International Journal of Retina and Vitreous*, vol. 5, no. 1, p. 15, Jun 2019. [Online]. Available: https://doi.org/10.1186/s40942-019-0165-z

[3] J. Yang, Z. Zhao, S. Shen, D. Zapp, M. Maier, K. Huang, N. Navab, and M. A. Nasseri, "Eyels: Shadow-guided instrument landing system for target approaching in robotic eye surgery," *IEEE Robotics and Automation Letters*, vol. 9, no. 4, pp. 3664–3671, 2024.

[4] A. Grzybowski and P. Kanclerz, "Early descriptions of vitreous surgery," *RETINA*, vol. 41, no. 7, 2021. [Online]. Available: https://journals.lww.com/retinajournal/fulltext/2021/07000/early_descriptions_of_vitreous_surgery.2.aspx

[5] H. Moon, D. Y. Lee, and D. H. Nam, "Trimanual technique using assistant-controlled light probe illumination and wide-angle viewing system in 23-gauge sutureless vitrectomy for diabetic tractional retinal detachment," *Ophthalmic Surgery, Lasers and Imaging Retina*, vol. 46, no. 1, pp. 73–76, 2015. [Online]. Available: https://journals.healio.com/doi/abs/10.3928/23258160-20150101-12

[6] G. Bamonte and P. R. van den Biesen, "Vitreous base visualisation through trans-scleral illumination with a standard 25-gauge light probe," *British Journal of Ophthalmology*, vol. 98, no. 2, pp. 281–283, 2014. [Online]. Available: https://bjo.bmj.com/content/98/2/281

[7] S. Dehghani, M. Sommersperger, P. Zhang, A. Martin-Gomez, B. Busam, P. Gehlbach, N. Navab, M. A. Nasseri, and I. Iordachita, "Robotic navigation autonomy for subretinal injection via intelligent real-time virtual ioct volume slicing," *arXiv preprint arXiv:2301.07204*, 2023.

[8] M. Zhou, X. Guo, M. Grimm, E. Lochner, Z. Jiang, A. Eslami, J. Ye, N. Navab, A. Knoll, and M. A. Nasseri, "Needle detection and localisation for robot-assisted subretinal injection using deep learning," *CAAI Transactions on Intelligence Technology*, 2023.

[9] M. Sommersperger, J. Weiss, M. A. Nasseri, P. Gehlbach, I. Iordachita, and N. Navab, "Real-time tool to layer distance estimation for robotic subretinal injection using intraoperative 4d oct," *Biomed. Opt. Express*, vol. 12, no. 2, pp. 1085–1104, Feb 2021. [Online]. Available: https://opg.optica.org/boe/abstract.cfm?URI=boe-12-2-1085

[10] P. Zhang, J. W. Kim, P. Gehlbach, I. Iordachita, and M. Kobilarov, "Autonomous needle navigation in retinal microsurgery: Evaluation in ex vivo porcine eyes," 2023. [Online]. Available: https://arxiv.org/abs/2301.11839

[11] B. Keller, M. Draelos, G. Tang, S. Farsiu, A. N. Kuo, K. Hauser, and J. A. Izatt, "Real-time corneal segmentation and 3d needle tracking in intrasurgical oct," *Biomedical optics express*, vol. 9, no. 6, pp. 2716–2732, 2018.

[12] J. P. Ehlers, A. Uchida, and S. K. Srivastava, "Intraoperative optical coherence tomography-compatible surgical instruments for real-time image-guided ophthalmic surgery," *British Journal of Ophthalmology*, vol. 101, no. 10, pp. 1306–1308, 2017. [Online]. Available: https://bjo.bmj.com/content/101/10/1306

[13] T. Asami, H. Terasaki, Y. Ito, T. Sugita, H. Kaneko, J. Nishiyama, H. Namiki, M. Kobayashi, and N. Nishizawa, "Development of a Fiber-Optic Optical Coherence Tomography Probe for Intraocular Use," *Investigative Ophthalmology & Visual Science*, vol. 57, no. 9, pp. OCT568–OCT574, 08 2016. [Online]. Available: https://doi.org/10.1167/iovs.15-18853

[14] S. Yang, J. N. Martel, L. A. Lobes, and C. N. Riviere, "Techniques for robot-aided intraocular surgery using monocular vision," *The International Journal of Robotics Research*, vol. 37, no. 8, p. 931–952, July 2018. [Online]. Available: http://dx.doi.org/10.1177/0278364918778352

[15] M. Zhou, J. Wu, A. Ebrahimi, N. Patel, Y. Liu, N. Navab, P. Gehlbach, A. Knoll, M. A. Nasseri, and I. Iordachita, "Spotlight-based 3d instrument guidance for autonomous task in robot-assisted retinal surgery," *IEEE Robotics and Automation Letters*, vol. 6, no. 4, pp. 7750–7757, 2021.

[16] T. C. Hutchens, A. Darafsheh, A. Fardad, A. N. Antoszyk, H. S. Ying, V. N. Astratov, and N. M. Fried, "Characterization of novel microsphere chain fiber optic tips for potential use in ophthalmic laser surgery," *Journal of Biomedical Optics*, vol. 17, no. 6, pp. 068 004–068 004, 2012.

[17] N. T. Clancy, D. Stoyanov, L. Maier-Hein, A. Groch, G.-Z. Yang, and D. S. Elson, "Spectrally encoded fiber-based structured lighting probe for intraoperative 3d imaging," *Biomed. Opt. Express*, vol. 2, no. 11, pp. 3119–3128, Nov 2011. [Online]. Available: https://opg.optica.org/boe/abstract.cfm?URI=boe-2-11-3119

[18] Y. Koyama, M. M. Marinho, M. Mitsuishi, and K. Harada, "Autonomous coordinated control of the light guide for positioning in vitreoretinal surgery," *IEEE Transactions on Medical Robotics and Bionics*, vol. 4, no. 1, pp. 156–171, 2022.

[19] C. He, E. Yang, N. Patel, A. Ebrahimi, M. Shahbazi, P. Gehlbach, and I. Iordachita, "Automatic light pipe actuating system for bimanual robot-assisted retinal surgery," *IEEE/ASME Transactions on Mechatronics*, vol. 25, no. 6, pp. 2846–2857, 2020.

[20] Y. Ida, N. Sugita, T. Ueta, Y. Tamaki, K. Tanimoto, and M. Mitsuishi, "Microsurgical robotic system for vitreoretinal surgery," *International Journal of Computer Assisted Radiology and Surgery*, vol. 7, no. 1, p. 27–34, May 2011. [Online]. Available: http://dx.doi.org/10.1007/s11548-011-0602-4

[21] K. Januschowski, C. Irigoyen, J. C. Pastor, G. K. Srivastava, M. R. Romano, H. Heimann, P. Stalmans, K. Van Keer, K. Boden, P. Szurman, and M. S. Spitzer, "Retinal toxicity of medical devices used during vitreoretinal surgery: A critical overview," *Ophthalmologica*, vol. 240, no. 4, p. 236–243, 2018. [Online]. Available: http://dx.doi.org/10.1159/000488504

[22] S. Charles, "Illumination and phototoxicity issues in vitreoretinal surgery," *Retina*, vol. 28, no. 1, p. 1–4, Jan. 2008. [Online]. Available: http://dx.doi.org/10.1097/IAE.0b013e318156e015

[23] G. Jocher, A. Chaurasia, and J. Qiu, "Ultralytics YOLO," Jan. 2023. [Online]. Available: https://github.com/ultralytics/ultralytics